Chapter 8

Calibration of Time Projection Chambers

Calibrating the Time Projection Chamber (TPC) is a crucial step to study and correct for physics processes and detector effects impacting the deposited charges on wire planes. Key processes affecting the production, propagation and detection of ionisation electrons were detailed in Chapter 3, including recombination, diffusion, electron attenuation and Space Charge Effect (SCE). These effects have been well-studied by other LArTPC experiments like MicroBooNE [1, 2], ArgoNeuT [3], and ICARUS [4, 5]. Their results have demonstrated an improvement in the spatial, temporal, and energy resolution of charge signals after correcting for these effects, illustrating the importance of calibration to achieve high precision measurements.

Two Monte Carlo (MC) studies within the scope of charge calibration are presented in this chapter, focusing on electron attenuation and recombination. The first study of electron lifetime measurement is presented in Section 8.1. The second study is an assessment of the impacts of delta ray fluctuations on recombination, given in Section 8.2. Finally, Section 8.3 concludes the chapter with some remarks.

8.1 Electron Lifetime Measurement

Drifting electrons can be captured by electronegative impurities present in liquid argon, as previously described in Section 3.3.1. The reduction of the number of charges collected on a wire can be modelled as an exponential decay function following Eq. 3.6, where the electron lifetime τ indicates the argon purity level of the detector. A higher electron lifetime corresponds to a higher purity and vice versa. The electron lifetime can be precisely measured and used to recover the original charge deposition on the wires.

At Short-Baseline Near Detector (SBND), there are several methods to measure the electron lifetime. Firstly, three purity monitors were installed, two inside the cryostat and one outside, which provide quick and real-time monitoring of the argon purity. Another method requires a dedicated extraction of electron lifetime using deposited charges as measured by the wires. This calibration procedure is often performed on a sample of cosmic muons that fully cross the drift distance of the TPC, known as *anode-to-cathode* cosmic tracks. Since they traverse the whole drift distance, they make a good sample to study the charge per unit length dQ/dx dependency on the drift distance. The MicroBooNE experiment also employed the same anode-to-cathode-crossing cosmic tracks to study and correct for position- and time-dependent response of their TPCs[1].

The study aims to develop a procedure to measure electron lifetime and investigate detector effects that can introduce biases on the lifetime, such as diffusion and SCE. Within the scope of this study, anode-to-cathode cosmic tracks were simulated to perform the lifetime measurement. The procedure for electron lifetime measurement is outlined in Section 8.1.1, followed by Section 8.1.2 describing biases in lifetime measurement due to detector effects.

8.1.1 Electron Lifetime Extraction Procedure

The electron lifetime measurement requires information on the charge per unit length dQ/dx and the respective drift time t_{drift} of that charge cluster arrived at the wire. The charge reconstruction follows the workflow described in Section 6.2, whilst additional calculation is required to deduce the drift time. The drift time is defined as:

$$t_{drift} = \frac{x}{v_d},$$

(8.1)

where x is the location the charge deposition in drift direction (x-axis) and v_d is the drift velocity. At SBND, the drift velocity is expected to be at 0.1563 cm/μs at an electric field of 0.5 kV/cm and temperature of 88.4 K. The drift time can be calculated using the time recorded by the TPC readout when a charge cluster arrives at a wire t_m which is defined as [6]:

$$t_m = t_0 - t_{trigger} + t_{drift},$$

(8.2)

where t_0 is the time when the particle enters the detector and $t_{trigger}$ is the time when the TPC readout is triggered. For a beam neutrino that triggers the TPC readout, the readout window is configured to align with when the beam arrives at the detector such that $t_{trigger} = $

t_0, as illustrated in Fig. 4.8 in Section 4.2.7. On the other hand, a cosmic muon can occur anytime within the readout window and the time when it enters the detector t_0 is unknown.

A *cathode stitching* process was developed by the ProtoDUNE and Pandora collaboration to determine the t_0 of cosmic muons that cross the cathode [6]. This can be applied to any LArTPC experiments that have two TPCs sharing the same cathode. Fig. 8.1 depicts the *stitching* process. The reconstruction algorithm begins with an initial and incorrect assumption of $t_0 = 0$ [6], so that two cosmic track segments, shown by the red and blue lines, appear at the wrong positions in both drift volumes. The algorithm then shifts the drift coordinate in each TPC by an equal and opposite amount until the two segments are *stitched* at the cathode, shown by the black line, to recover the correct t_0. This method has been implemented in the reconstruction workflow of SBND, and it was applied to reconstruct the sample of anode-to-cathode-crossing tracks in this study.
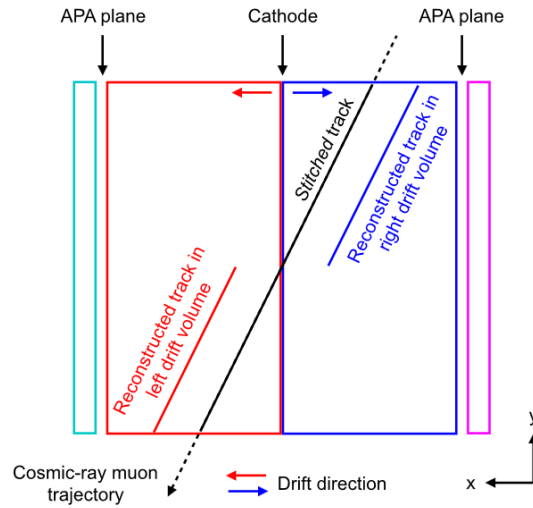

Fig. 8.1 Diagram depicting the cathode stitching process to determine the t_0 of cathode-crossing track [6].

The next step in the lifetime extraction procedure was to plot the charge per unit length dQ/dx in bins of the drift time t_{drift}. Fig. 8.2 shows an example dQ/dx profile in the drift time bin from 0.925 to 0.95 ms. A Landau-Gaussian convolution is fitted to the profile to extract the Most Probable Value (MPV) of dQ/dx [7]. This process was repeated for every drift time bin across the full drift distance of the TPC.

Fig. 8.3 shows the MPV dQ/dx as a function of drift time, for TPC 0 (east) and 1 (west) of SBND. Bins of drift time less than 0.25 ms and larger than 1.15 ms were excluded due to the close proximity to the anode and cathode respectively, which can introduce some boundary effects. The MPV dQ/dx distribution is fitted with Eq. 3.6 to determine the electron lifetime

constant. The MC sample input to Fig. 8.3 was simulated with a lifetime of 10 ms and no detector effects enabled to validate the procedure. The lifetimes were determined to be 10.12 ± 0.24 and 10.40 ± 0.29 ms, for TPC 0 and 1 respectively, showing a good agreement between the result and the simulation.
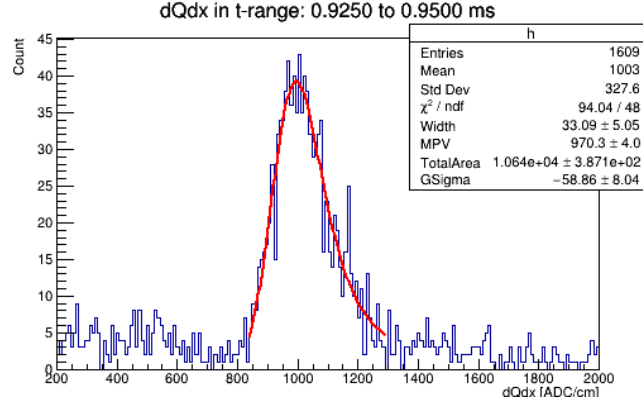
Fig. 8.2 Example of a dQ/dx profile in a drift time bin of 0.925–0.95 ms, fitted with a Landau-Gaussian convolution.
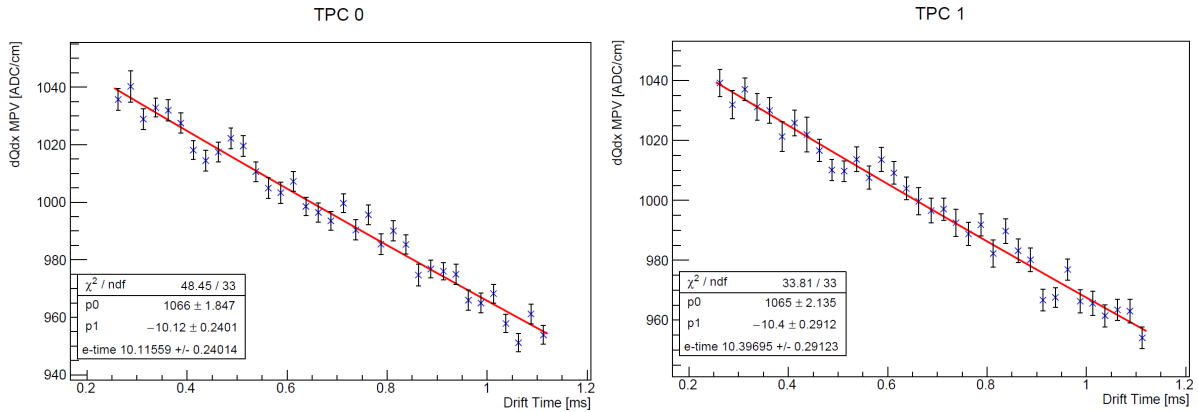
Fig. 8.3 MPV dQ/dx as a function of drift time, fitted with an exponential function.

8.1.2 Bias Study From Diffusion and Space Charge Effects

Some detector effects can introduce biases to the electron lifetime measurement, specifically those that can influence the propagation path of drifting electrons such as diffusion and SCE. Diffusion can smear both spatial and temporal resolution of the drifting electrons, and consequently the number of wires seen by the charge and the arrival time of charge measured by the wires. Meanwhile, SCE impacts both the amplitude of the measured charge

as well as the temporal and spatial resolution due to electric field distortion. In view of this, a study was undertaken to understand how each effect introduces biases to the measurement of electron lifetime.

Three dedicated MC samples were simulated: (1) No SCE nor diffusion enabled, (2) only diffusion enabled and (3) only SCE enabled. In the diffusion-only MC sample, the longitudinal diffusion coefficient was set at $D_L = 4.0$ cm^2/s, as measured by MicroBooNE [8], and the transverse diffusion coefficient was set at $D_T = 8.8$ cm^2/s, as measured by ProtoDUNE [9] (See Section 3.3.1 Chapter 3). In the SCE-only MC sample, the simulation of electric field distortion follows the description in Ref. [10].

Biases in the lifetime compared to the simulated lifetime are shown in Fig. 8.4, for two simulated electron lifetimes at 3 ms (top) and 10 ms (bottom). When no detector effects are enabled in the simulation, the determined lifetimes are very similar to the simulated lifetimes, with negative biases well below the 2% level. When either diffusion or SCE was enabled in the simulation, positive biases in the lifetimes can be seen. Biases due to diffusion are at ~ 2% and ~ 4% for the simulated lifetimes of 3 ms and 10 ms respectively. On the other hand, biases due to SCE are higher at ~ 5% and ~ 22% at the 3 ms and 10 ms lifetime. The observed biases are also consistent across the two TPC volumes of SBND.

The first observation is that the magnitude of the biases due to SCE is much greater than due to diffusion at both simulated lifetimes. This is consistent with the observations from an electron lifetime measurement carried out by MicroBooNE [2]. The paper demonstrated that both SCE and the transverse component of diffusion cause biases in the lifetime, however, biases due to transverse diffusion are smaller in magnitude than SCE. The paper also pointed out that the longitudinal component of diffusion causes insignificant biases in the lifetime.

The second observation is that the longer the lifetime, the larger the biases as compared between the lifetimes at 3 ms and 10 ms. This is most likely due to the precision of this method worsening with increasing lifetimes. Larger lifetime leads to a more uniform dQ/dx distribution across the drift distance, and thus, fitting an exponential function can become less reliable.

Since the results of this study, an investigation at the ICARUS experiment demonstrated that transverse diffusion breaks down the Landau-Gaussian MPV approximation of the measured charge [5], which was employed in this study. This is due to transverse diffusion smearing the charge cluster across multiple wires, resulting in a shift in the MPV value. The paper recommends using an averaged dQ/dx from a group of wires instead of dQ/dx from a single wire to mitigate the effect. The suggestion has now been implemented at SBND.
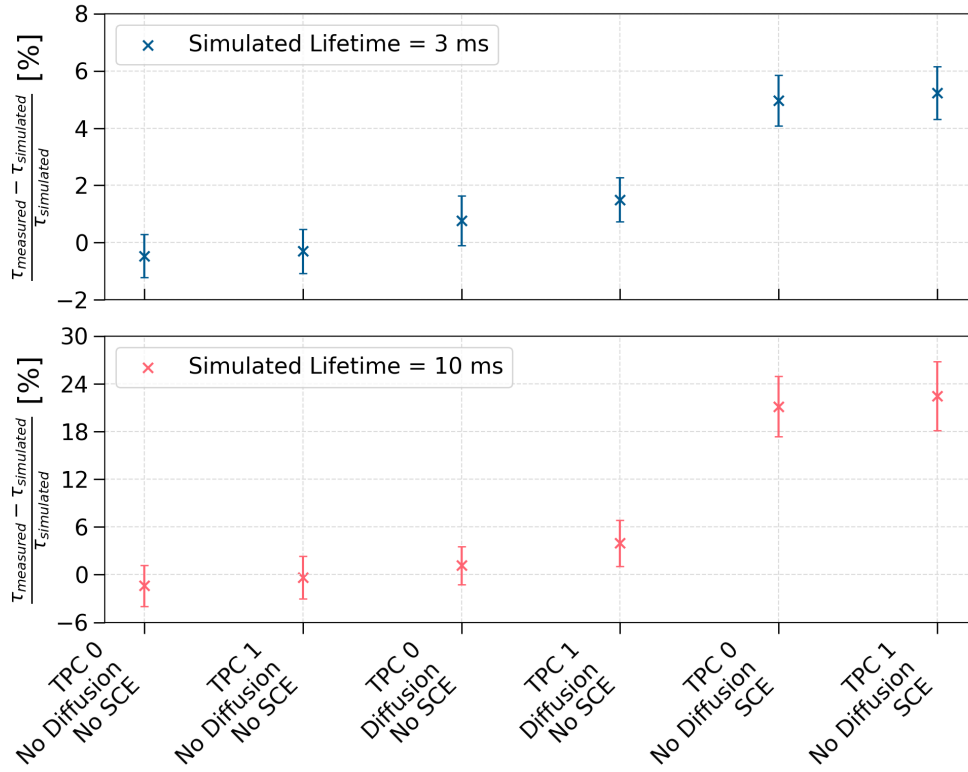
Fig. 8.4 Biases in electron lifetimes compared to the simulated values at 3 ms (top) and 10 ms (bottom).

The study presented here demonstrates a method to measure electron lifetime using a sample of anode-to-cathode crossing cosmic tracks. These tracks have the advantage of spanning over a full drift distance and a reconstructable t_0 time tagging when the particle enters the detector. The electron lifetime measured by this method is the most affected by SCE, followed by diffusion, which is consistent with the results from MicroBooNE. This procedure has now been replicated in preparation for the calibration run of SBND at the time of writing. A trigger requiring coincidence in the east and west CRT wall was deployed to produce dedicated samples containing crossing cosmic muon tracks that can be used for electron lifetime measurement.

8.2   Delta Ray Fluctuations on Recombination Simulation

Recombination is a physics process that drives the charge and light yield as previously described in Section 3.2.3. SBND currently employs the Modified Box (ModBox) model for simulating recombination, with experimentally-derived parameters from ArgoNeuT [3]. The

model approximates the recombination probability based on a cylindrical column surrounding a track-like charge deposition, effectively accounting for microphysics processes along the track. This approximation has proven to work well for the MeV to GeV-scale interactions, however, it breaks down at the keV-scale.

Delta rays are microphysics processes that can affect recombination, highlighted by NEST [11] and ArgoNeuT [3] collaborations. They are knock-out electrons with low energy but high energy loss per unit length dE/dx. As shown in Fig. 8.5, delta rays are short tracks produced along a longer primary track, in this case, a cosmic muon. Due to their high dE/dx, they are associated with a smaller recombination factor R (See Fig. 3.6 Section 3.2.3). A smaller R corresponds to a smaller probability of ionisation electrons surviving recombination. As a result, delta rays can lead to non-linear fluctuations in recombination that is not well-described by the ModBox model.

This study is motivated to asses the impacts of delta ray fluctuations on the simulation of recombination, and consequently, the charge to energy loss conversion of different particle types. An overview of the simulation framework of delta rays and recombination is given in Section 8.2.1.In following, Section 8.2.2 and 8.2.3 provides a description of the delta ray impacts on the recombination magnitude and smearing respectively. A summary of recombination studies carried out by the ICARUS collaboration is presented in Section 8.2.4.
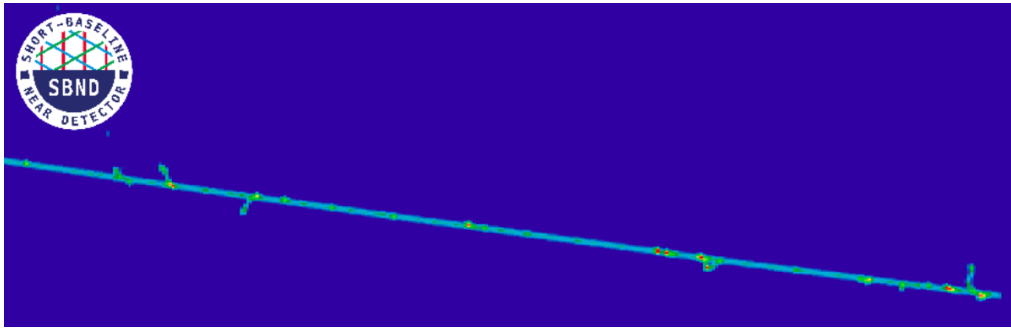
Fig. 8.5 Event display of a simulated cosmic muon track segment, with many delta rays produced along the primary track.

8.2.1   Simulation of Delta Rays and Recombination

Delta rays and recombination are simulated as part of the particle propagation simulation performed by the Geant4 toolkit [12], with details provided in Section 5.4.1. The simulation propagates the primary particle step by step and applies physics processes at each step of length dx. Particularly, this study focuses on the energy loss due to ionisation. It is simulated

as two dependent processes: (1) a continuous energy loss dE of the primary particle along the step dx and (2) a discrete energy loss dE at the end of the step producing delta rays [12].

The continuous energy loss of the primary particle is simulated by Geant4 using complementary models depending on the particle Kinetic Energy (KE) [13]. For particles with KE > 2 MeV, the Bethe-Bloch formalism [7], detailed in Section 3.2.1, is used to compute the mean dE/dx. In the intermediate KE range range < 2 MeV, simulation models parameterised on data from Ref. [14] and Ref. [15] are implemented. In the low KE < 1 keV, Geant4 uses the free electron gas model since no data is available.

The discrete energy loss to produce delta rays is determined by a user-defined energy threshold. The energy threshold defines the lower limit of the KE of delta rays so that only delta rays with sufficient energy can be produced. This is to suppress the simulation of all low energy delta rays that would exhaust computation resources. This also means that the energy of the non-produced delta rays is transferred to the continuous energy loss of the primary particle. This is equivalent to setting the energy threshold as the upper limit for the primary particle so that its mean continuous energy loss is less than the threshold.

In Geant4 terminology, the energy threshold is also known as the secondary production threshold, where the minimum KE requirement for delta ray production is defined as the minimum distance the generated delta ray must be able to traverse in a given material. These thresholds will be referred to as *delta ray thresholds* in short from this point onwards in this study. Moreover, the maximum length dx that the particle can propagate per step is configured as 0.3 mm, one order of magnitude smaller than the wire pitch of 3 mm. This setup allows for a feasible computation of generating delta rays.

For each step dx, the number of electron-ion pairs is calculated by dividing the continuous energy loss dE by the ionisation work function of argon W_{ion} = 23.6 eV [16]. Then, the recombination factor R is applied to the number of electron-ion pairs according to the charge-light anti-correlation described by Eq. 3.2 and 3.3, to determine the final charge and light yield resulting from the step dx. Using the ModBox formalism, R is computed as [3]:

$$R = \frac{\log\left(\alpha + \left(\beta \cdot dE/dx\right)/\varepsilon\right)}{\left(\beta \cdot dE/dx\right)/\varepsilon}, \tag{8.3}$$

where ε (kV/cm) is the electric field at the position of the step, dE/dx (MeV/cm) is the energy loss per unit length, and parameters $\alpha = 0.93 \pm 0.02$ and $\beta = 0.212 \pm 0.002$ (kV/cm)(g/cm^2)/MeV were experimentally derived by ArgoNeuT [3]. Eq. 8.3 is plotted in Fig. 3.6 Section 3.2.3. It is important to note that R is dependent on the electric field and therefore can be influenced by local distortions of the field.

The simulation of delta rays and recombination described here gives rise to some concerns. The first concern is the assumption of a *universal* recombination factor R. The parameters α and β were measured by ArgoNeuT using a stopping proton sample, and wire planes with a pitch of 3 mm [3]. Nonetheless, they are applied to any type of ionising particles, which can influence the local ionisation density differently. Secondly, the delta ray thresholds remove low energy electrons in simulation. However, they are produced in reality and can affect recombination at a local scale.

The study was set up to address the individual concerns outlined above to better understand their impacts on recombination. Identical MC samples of muons and protons were simulated to investigate if recombination is particle-dependent. The particles were generated with a fixed energy of 1 GeV, uniform in positional and angular distributions. The Geant4 simulation was configured such that the particle can only deposit energy via ionisation. The *true* energy per unit length dE/dx was computed from the *true* number of electrons per unit length dQ/dx, where *true* indicates no detector simulations were applied. The computation follows the ModBox formalism for charge to energy loss conversion as [3]:

$$\frac{dE}{dx} = \frac{1}{\beta} \left[\exp\left(\beta W_{ion} \frac{dQ}{dx} \right) - \alpha \right],$$

(8.4)

where parameters are the same as Eq. 8.3. For each particle type, a range of delta ray thresholds were simulated. The largest value, and also the current value being used by SBND, was set at 700 μm, equivalent to delta rays with a minimum KE of 273 keV. The smallest threshold was 1 μm, enabling the simulation of delta rays with KE as low as 1 keV. This variation was chosen to study the impacts due to delta ray fluctuations.

8.2.2 Impacts of Delta Ray Fluctuations On Recombination Magnitude

Fig. 8.6 shows the simulated charge to energy loss conversion, dQ/dx to dE/dx, for protons at the delta ray threshold of 700 μm and 1 μm. The distribution was plotted for the proton residual range from 1 cm to 90 cm to cover the full track length. The proton dE/dx ranges from 2 MeV/cm to 18 MeV/cm, allowing for the examination of delta ray fluctuation impacts at both low and high parts of the dE/dx spectrum. For the delta ray threshold of 700 μm shown in Fig. 8.6a, the distribution precisely follows the ModBox model with the ArgoNeuT parameters defined in Eq. 8.4. A good agreement is expected since the simulation of SBND is similar to that of ArgoNeuT [3].

However, for the delta ray threshold of 1 μm shown in Fig. 8.6b, deviations away from the ModBox model occur, such that the distribution shifts at both low and high parts of the dE/dx specturm. Lowering the delta ray threshold leads to more energy loss carried by the delta rays instead of the primary proton, and thus, delta rays have a greater influence on recombination. At the low dE/dx spectrum of the proton, delta rays have higher dE/dx and a smaller recombination factor R than that of the proton. This results in the *effective recombination factor* being reduced, decreasing dQ/dx at the same value of dE/dx. The opposite effect is seen at the high dE/dx spectrum of the proton, where dQ/dx is higher than the ModBox model. This indicates that the effective recombination factor increases, that accounts for both the primary proton and delta rays.

(a) 700 μm

(b) 1 μm
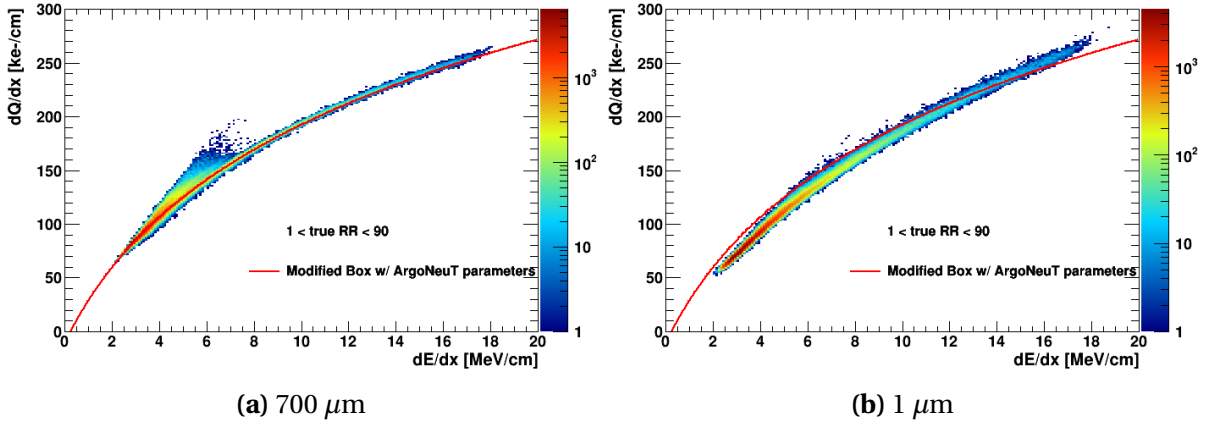
Fig. 8.6 dQ/dx as a function of dE/dx for a 1 GeV proton at the delta ray threshold of (a) 700 μm and (b) 1 μm.

(a)

(b)
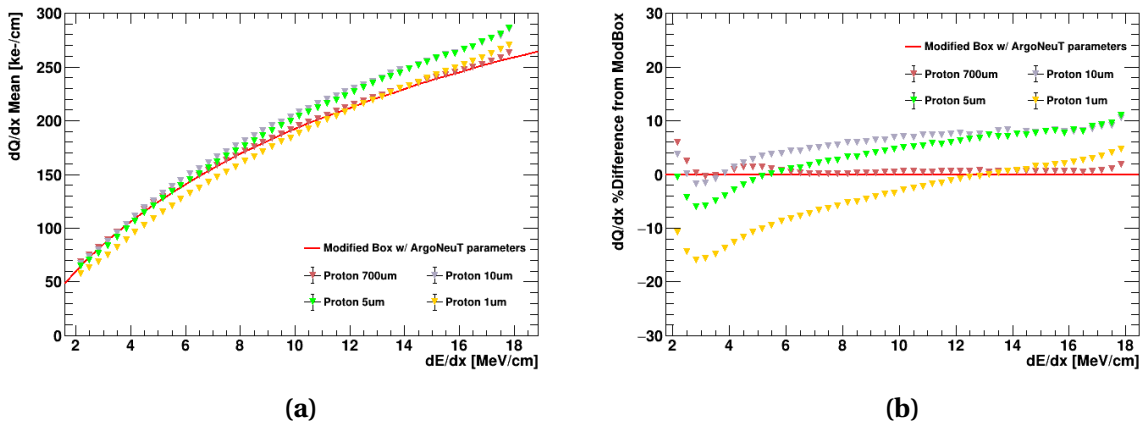
Fig. 8.7 (a) Mean dQ/dx and (b) its percentage difference relative to the Mod-Box model as a function of dE/dx for a 1 GeV proton.
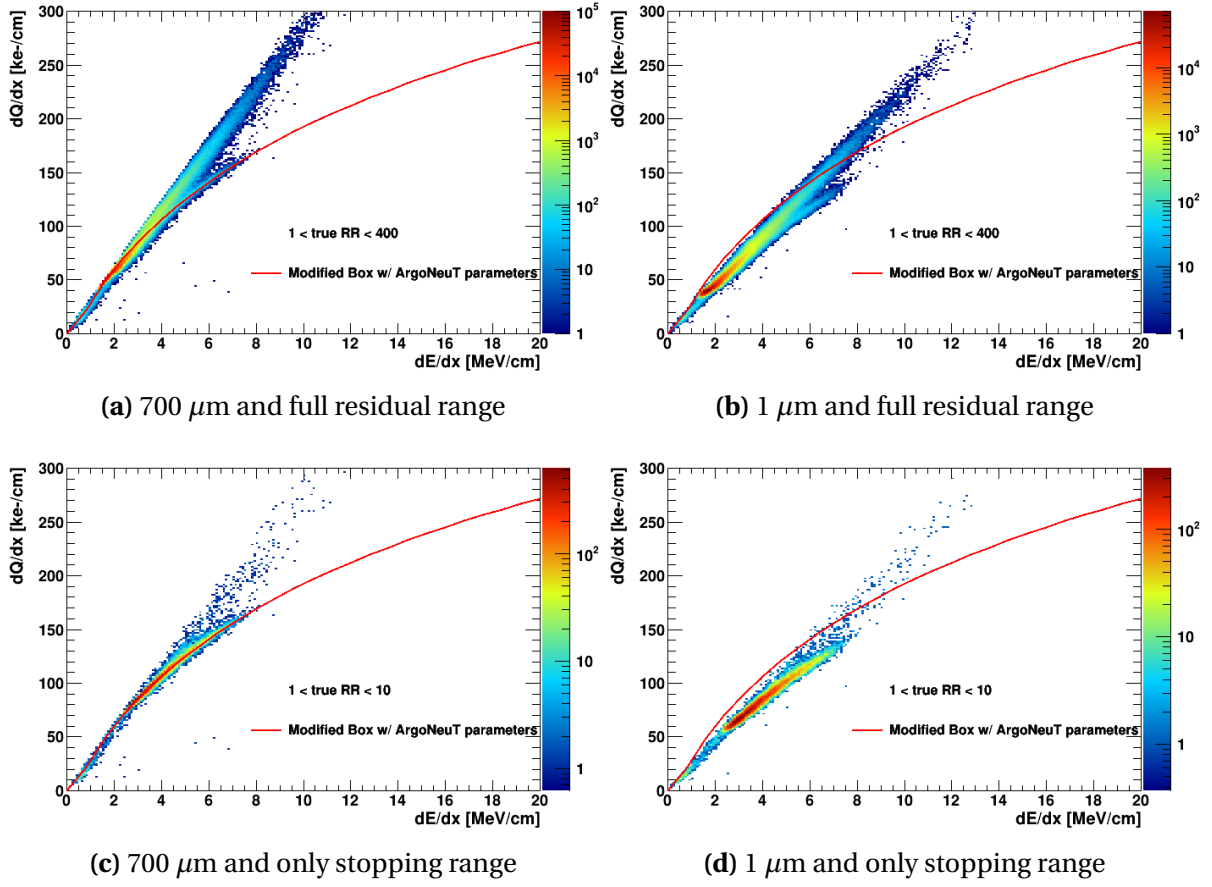
The proton charge to energy loss conversion at the thresholds of 700, 10, 5, and 1 μm, equivalent to delta rays with a minimum KE of 272.58, 14.60, 2.58, 1.06, and 0.99 keV are shown in Fig. 8.7. To compare dQ/dx quantitatively at the same dE/dx bin, the mean dQ/dx was calculated per dE/dx bin as shown in Fig. 8.7a. The percentage difference of the mean dQ/dx relative to the ModBox model is depicted in Fig. 8.7b to quantify the magnitude of the differences.

Lowering the KE of delta rays results in two key trends. Firstly, the dE/dx position at which the proton charge to energy loss conversion shifts in upward/downward directions, increases with lower delta ray KE. This shift position can be seen in Fig. 8.7b. Secondly, the magnitude of the deviations depends on the delta ray threshold. At low $dE/dx <\sim$ 8 MeV/cm, the effective recombination is reduced the most at the 1 μm threshold, as shown in yellow. At high $dE/dx >\sim$ 8 MeV/cm, the effective recombination is the highest at the 5 μm threshold, as shown in green. This is evidence that delta ray fluctuations can greatly influence the proton charge to energy loss conversion. The more energy loss is carried away by very low KE delta rays, the more distorted the charge to energy scale becomes.

The charge to energy loss conversion for muons is plotted in Fig. 8.8, for the delta ray threshold at 700 μm and 1 μm. Fig. 8.8a and 8.8b contain the full muon residual range, covering the track length 1–400 cm. Two distinct distributions can be seen here, one linear from the Minimum Ionising Particle (MIP) region, and another one that follows the ModBox model indicating the stopping region. The linear charge to energy loss conversion of MIP muons has been well-observed by LArTPC experiments, including MicroBooNE [1] and ICARUS [4].

To examine only the stopping region, a residual range requirement of less than 10 cm was applied, as shown in Fig. 8.8c and 8.8d. The effects of lowering the delta ray can be seen by comparing the two figures. The same behaviour as protons at the same low $dE/dx <\sim$ 8 MeV/cm is observed, where low energetic delta rays result in a smaller effective recombination factor, reducing dQ/dx at the same value of dE/dx.

The mean dQ/dx of muons and its percentage difference relative to the ModBox model are also shown in Fig. 8.9, at various values of delta thresholds. Similar to protons, the magnitude of the effective recombination reduction increases with lower delta ray KE. The recombination factor is also the most affected at the threshold of 1 μm, as shown in red. It is also important to note that the magnitude of the reduction is larger for muons compared to protons, which is likely due to the amount of delta rays produced by each particle type. For instance, at the same dE/dx of 3 MeV/cm and the threshold of 1 μm, the percentage difference is at $\sim$ 24% for muons and $\sim$ 16% for protons.

(a) 700 μm and full residual range

(b) 1 μm and full residual range

(c) 700 μm and only stopping range

(d) 1 μm and only stopping range

Fig. 8.8 dQ/dx as a function of dE/dx for a 1 GeV muon at the delta ray threshold of 700 μm (left) and 1 μm (right) and for the full residual range (top) and only the stopping range (bottom).

(a)

(b)
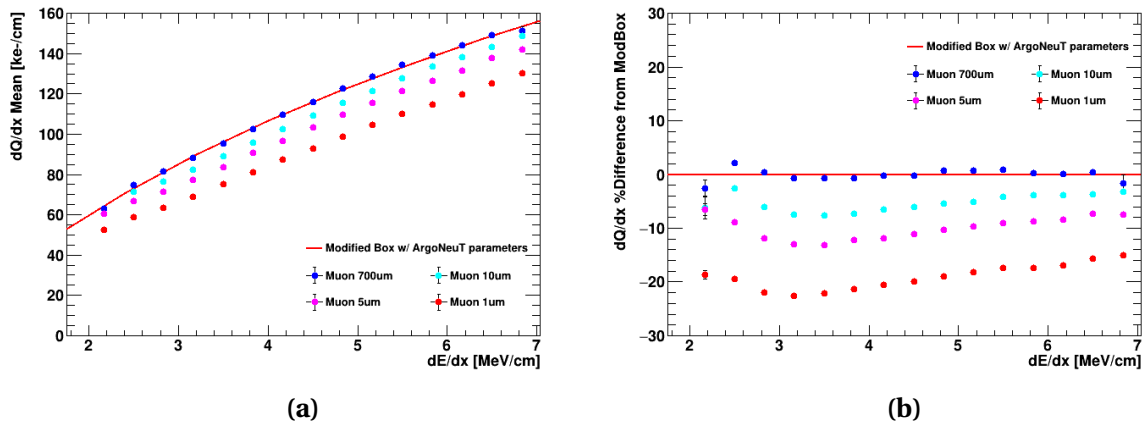
Fig. 8.9 (a) Mean dQ/dx and (b) its percentage difference relative to the Mod-Box model as a function of dE/dx for a 1 GeV muon.

The study here demonstrates that fluctuations of delta rays can affect recombination. Delta rays have a different dE/dx compared to the primary particle and therefore, can influence the effective recombination factor. At low $dE/dx <\sim 8$ MeV/cm, this results in an overall reduction of recombination. Meanwhile, at high $dE/dx >\sim 8$ MeV/cm, delta rays can increase the effective recombination factor. This leads to a distortion of the observed charge to energy loss conversion of a particle. The magnitude of recombination is more significant for muons than protons.
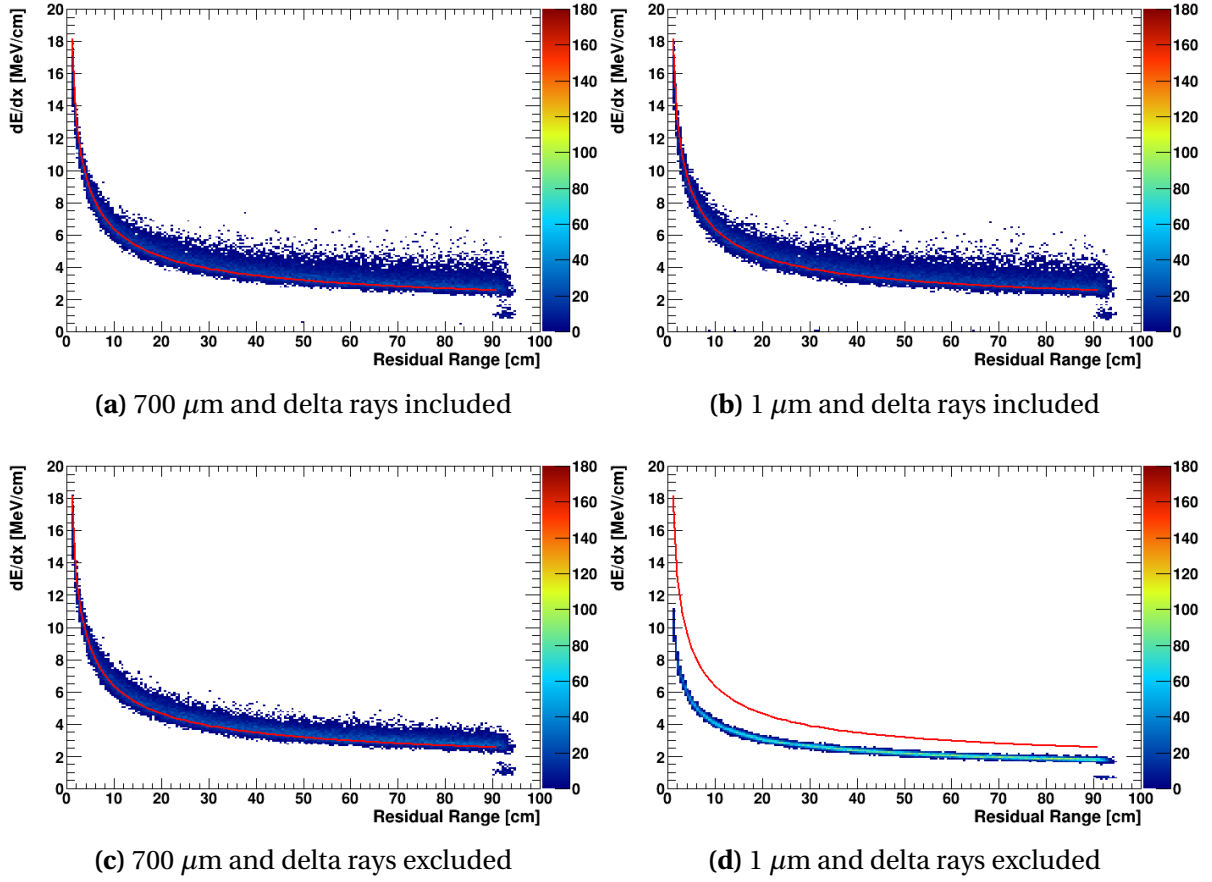
8.2.3 Impacts of Delta Ray Fluctuations On Recombination Smearing

Delta ray fluctuations affect not only the magnitude of the recombination factor but also its smearing, and consequently, the smearing of the charge to energy loss conversion. To disentangle how the Geant4 toolkit handles the smearing due to delta rays, an additional study was carried out in which the energy deposition of the primary particle was isolated from delta rays.

Fig. 8.10 shows the simulated dE/dx of the primary proton as a function of its residual range, compared against the Landau-Vavilov distribution [7]. Energy loss due to delta rays is included in the top two plots, Fig. 8.10a and Fig. 8.10b, for the delta thresholds of 700 μm and 1 μm. Meanwhile, the bottom two plots, Fig. 8.10c and Fig. 8.10d, only include the energy loss of the primary proton and do not account for the energy loss of delta rays. The same set of plots for the case of muons are also shown in Fig. 8.11.

When delta rays are included in the energy loss, the dE/dx distribution agrees with the Landau-Vavilov distribution with some smearing in dE/dx across all residual range bins. The energy distributions are indistinguishable between the delta ray threshold of 700 μm and 1 μm. This can be seen for both protons, comparing Fig. 8.10a and Fig. 8.10b, and muons, comparing Fig. 8.11a and 8.11b. The behaviour is expected since the total energy loss of the primary particle and the delta rays must stay the same regardless of the delta ray threshold. Moreover, comparing the protons and muons, including delta rays in the total energy loss introduces greater smearing in the dE/dx distribution for muons than protons.

When delta rays are excluded in the energy loss, some noticeable effects can be seen. At the threshold at 700 μm, the dE/dx distribution of only the primary particle but no delta rays still follows closely the Landau-Vavilov distribution, similarly to the dE/dx distribution containing both the primary particle and delta ray energy loss. This can be seen comparing Fig. 8.10a and Fig. 8.10c for protons, and comparing Fig. 8.11a and 8.11c for muons. However, less smearing in dE/dx is observed when delta rays are excluded in the energy
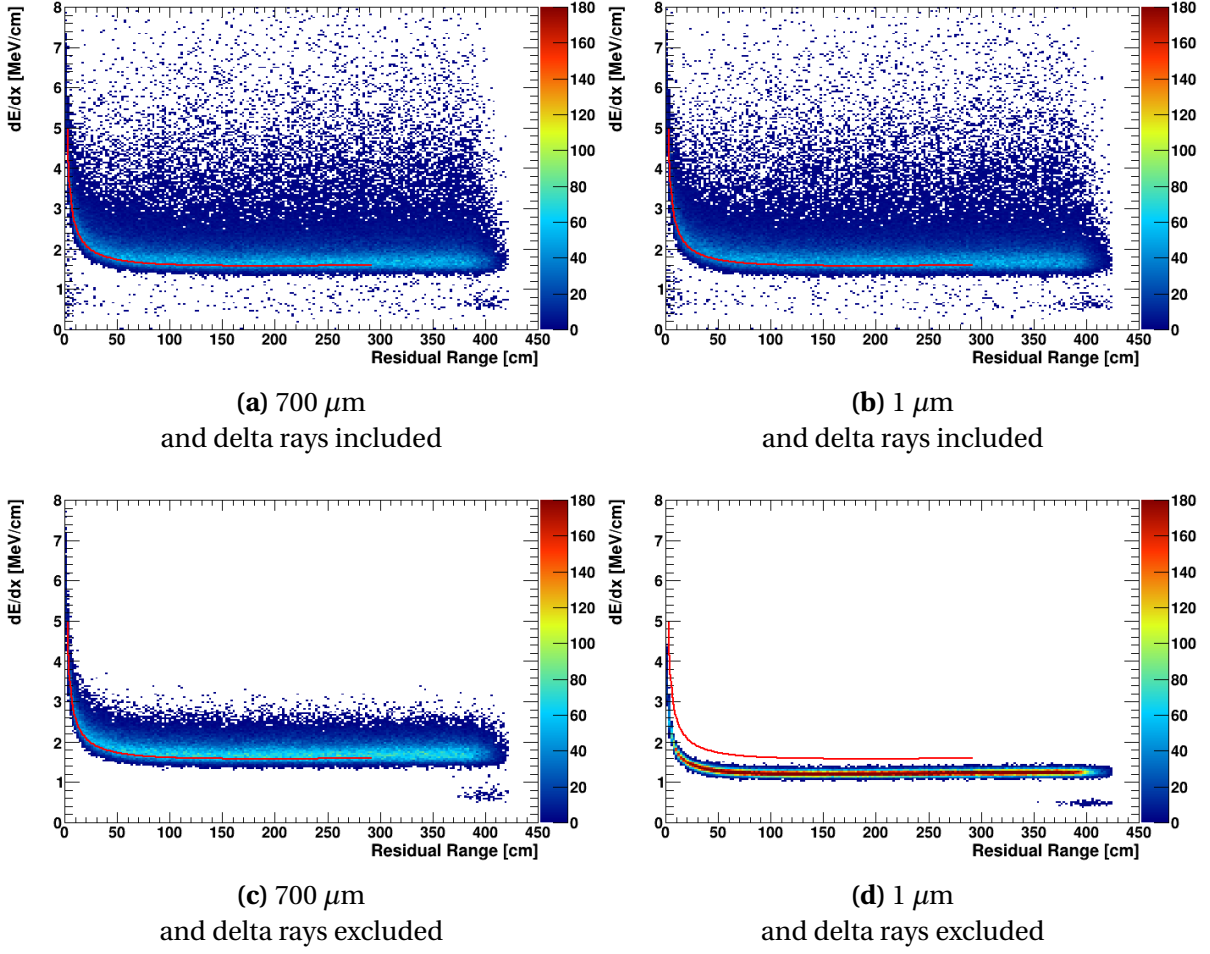
(a) 700 μm and delta rays included

(b) 1 μm and delta rays included

(c) 700 μm and delta rays excluded

(d) 1 μm and delta rays excluded

Fig. 8.10 dE/dx as a function of residual range for a 1 GeV proton at the delta ray threshold of 700 μm (left) and 1 μm (right), including (top) and excluding (bottom) the energy loss of delta rays.

loss, especially visible in Fig. 8.11c for muons. At this configuration, the majority of the energy loss is carried away by the primary particle, and Geant4 already accounts for delta ray fluctuations when sampling its mean energy loss [12]. Introducing energy loss by delta rays only adds some additional smearing to the total dE/dx distribution.

On the other hand, when the delta ray threshold is set to 1 μm and no delta rays are considered, the dE/dx distribution of only the primary particle becomes narrow without any smearing and fails to follow the Landau-Vavilov distribution. This can be seen in Fig. 8.10d for protons and Fig. 8.11d for muons. Isolating only the energy deposition of the primary particle is equivalent to observing a *bare* proton or muon track without any delta rays produced along its path, which has not been experimentally measured before. In this case, the stopping power distribution of the primary particle is computed by Geant4 using

(a) 700 μm
and delta rays included

(b) 1 μm
and delta rays included

(c) 700 μm
and delta rays excluded

(d) 1 μm
and delta rays excluded

Fig. 8.11 dE/dx as a function of residual range for a 1 GeV muon at the delta ray threshold of 700 μm (left) and 1 μm (right), including (top) and excluding (bottom) the energy loss of delta rays.

interpolation instead of using data-based parametrisation [12]. This potentially leads to inaccuracy in simulating the energy loss due to ionisation.

This study here demonstrates another effect of delta ray fluctuations on recombination. Having a different dE/dx to the primary particle also means that delta rays can smear the observed charge to energy loss conversion. The amount of smearing vary differently between protons and muons, where including delta rays in the energy loss lead to more smearing in the dE/dx distribution for muons than protons. Combining with the results from Section 8.2.2, this suggests a need for a particle-dependent recombination factor.

8.2.4 Recombination Studies From The ICARUS Experiment

A very similar study was carried out by the ICARUS collaboration in 2004 in Italy, to investigate delta ray fluctuations impacting recombination and also to compare against their experimental data [4]. The result is shown in Fig. 8.12, showing the recombination factor as a function of the delta ray threshold in MC. The dotted line is the expectation for a MIP muon with a KE of 250 MeV. The recombination factor increases with the threshold and peaks at ~ 0.7, then decreases with higher thresholds. This result is similar to the observation of the study described above, where the effective recombination factor reduces at small values of delta ray thresholds.

The ICARUS collaboration proposed a few different approaches toward the simulation of recombination so that delta ray fluctuations can be more accurately simulated [4]. The first approach was to simulate *as microscopic as possible*, by simulating delta rays with KE $\mathcal{O}(1\ \text{eV})$ and range $\mathcal{O}(10\ \text{nm})$. However, they concluded that this approach was not feasible. Firstly, the effective recombination factor of a particle always contains effects due to delta rays, and secondly, computing resources are limited. Another proposal was an empirical approach, to choose the best delta ray threshold in simulation to reproduce the data with a reasonable computing consumption. This number was found to be 3 μm, equivalent to simulating delta rays having a KE as low as 10 keV.

Also recently from the ICARUS collaboration, now with the detector relocated to Fermilab, a study in 2024 of recombination showed a clear dependence of recombination on the angle
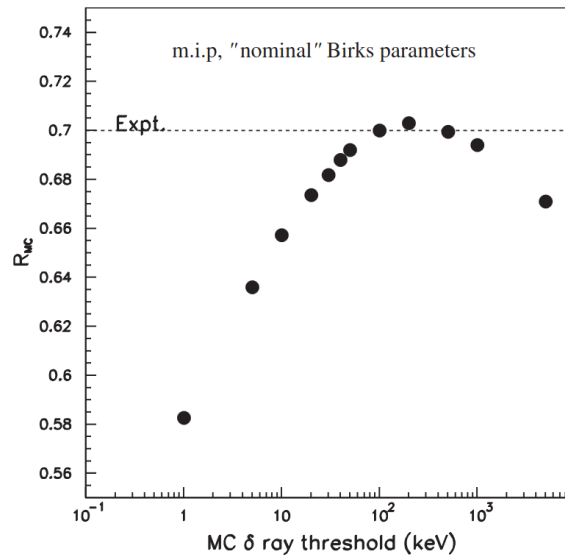
Fig. 8.12 Recombination factor as a function of the delta ray threshold [4].

116

of the particle track to the drift electric field [**TODO**]. A new ellipsoid modified box model of recombination was proposed and able to describe the data across all measured angles. This result has significantly improved the observed charge to energy loss conversion of a particle, which is critical for particle identification of an LArTPC.

These results from the ICARUS collaboration have collectively enhanced the understanding of recombination, as well as guided how to model recombination at SBND. In the scope of calibrating the SBND detector, it is highly recommended to follow a data-driven approach such that the simulation of delta rays and recombination should be tuned to best match the observed data, as done by earlier experiments like ICARUS and ArgoNeuT.

8.3   Concluding Remarks

Two studies within the scope of calibrating ionisation electron signals were presented. The first study described a procedure to measure electron lifetime using anode-to-cathode crossing cosmic muons and quantify biases in the acquired lifetime due to SCE and diffusion. The second study examined the simulation of delta rays and recombination, and how delta ray fluctuations can impact the effective recombination factor and consequently, the charge to energy loss conversion of a particle. These studies help understanding how different detector effects and physics processes can impact the charge depositions on wires, which can be pinned down and corrected for. This calibration process enables high precision measurements, which are essential for any physics analysis at SBND, including the search for HNLs. The following Chapter 9 focuses on the selection of HNLs, of which many reconstruction variables describing the calorimetry and topology of a particle relies on having an accurate charge information.

References

[1] C. Adams et al. (MicroBooNE), "Calibration of the charge and energy loss per unit length of the MicroBooNE liquid argon time projection chamber using muons and protons", JINST **15**, P03022 (2020).

[2] R. Acciarri et al. (MicroBooNE,), "A Measurement of the Attenuation of Drifting Electrons in the MicroBooNE LArTPC", 10.2172/1573054 (2017).

[3] R. Acciarri et al., "A study of electron recombination using highly ionizing particles in the ArgoNeuT Liquid Argon TPC", Journal of Instrumentation **8**, P08005 (2013).

[4] S. Amoruso et al., "Study of electron recombination in liquid argon with the ICARUS TPC", Nuclear Instruments and Methods in Physics Research Section A: Accelerators, Spectrometers, Detectors and Associated Equipment **523**, 275–286 (2004).

[5] G. Putnam et al., "Effect of diffusion on the peak value of energy loss observed in a LArTPC", JINST **17**, P10044 (2022).

[6] A. A. Abud et al. (DUNE Collaboration), "Reconstruction of interactions in the ProtoDUNE-SP detector with Pandora", The European Physical Journal C **83**, 618 (2023).

[7] D. E. Groom et al., "Passage of particles through matter", The European Physical Journal C - Particles and Fields **15**, 163–173 (2000).

[8] P. Abratenko et al. (MicroBooNE), "Measurement of the longitudinal diffusion of ionization electrons in the MicroBooNE detector", Journal of Instrumentation **16**, P09025 (2021).

[9] B. Abi et al., "First results on ProtoDUNE-SP liquid argon time projection chamber performance from a beam test at the CERN Neutrino Platform", Journal of Instrumentation **15**, P12004 (2020).

[10] M. Mooney, "The MicroBooNE Experiment and the Impact of Space Charge Effects", in Meeting of the APS Division of Particles and Fields (Nov. 2015).

[11] M. Szydagis et al., "A Review of Basic Energy Reconstruction Techniques in Liquid Xenon and Argon Detectors for Dark Matter and Neutrino Physics Using NEST", Instruments **5**, 13 (2021).

[12] S. Agostinelli et al., "Geant4—a simulation toolkit", Nuclear Instruments and Methods in Physics Research Section A: Accelerators, Spectrometers, Detectors and Associated Equipment **506**, 250–303 (2003).

[13] S. Giani et al., "GEANT4 simulation of energy losses of ions", (1999).

[14] H. H. Andersen et al., *Hydrogen Stopping powers and ranges in all elements* (Pergamon Press, United States, 1977).

[15] "ICRU Report 49, Stopping Power and Ranges for Protons and Alpha Particles", Journal of the ICRU **os-25** (1993).

[16] M. Miyajima et al., "Average energy expended per ion pair in liquid argon", Phys. Rev. A **9**, 1438–1443 (1974).